Geometry of Miura-Folded Meta-Materials — Supplementary Information

Mark Schenk, Simon D. Guest *

*Cambridge University Engineering Department, Trumpington Street, CB2 1PZ, Cambridge, United Kingdom

S1. Facet Bending

To model out-of-plane deformations of the *Miura-ori* sheet, facet bending must be taken into account. This is modelled by introducing a diagonal fold line to the facets. To first order approximation, the orientation of the additional diagonal fold line does not affect the kinematics, as all other nodal displacements are of higher-than-first order, as illustrated in Fig. 1. In a stiffness analysis, however, the length of the fold line will affect the mechanical response. In our analysis the shorter diagonal was selected, based on energetic considerations as well as observations of physical models.
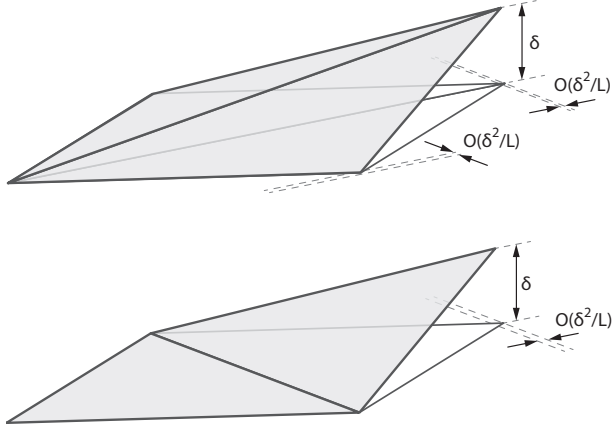

Fig. 1: The facet bending of the *Miura* unit cell can be modelled by introducing a diagonal fold line. To first order approximation the choice of diagonal does not matter, as all other nodal displacements are of higher order and will not feature in the analysis (δ is an out-of-plane deformation, and L is an in-plane dimension).

S2. Numerical Model

In our analysis the *Miura-ori* sheet is modelled as a spherically-jointed framework: the fold lines are represented by bars, and the vertices by frictionless joints. The underlying assumption is that the fold lines remain straight during deformation. In physical folded sheets one may observe deformations of the fold lines, for example in the folded hyperbolic paraboloid ('hypar') [1], but for strictly developable deformations the geodesic curvature of a fold line must be preserved [2].

The analysis of pin-jointed frameworks is well-established in structural mechanics. Its mechanical properties can be described by three linearised matrix equations: equilibrium, compatibility and material properties [3].

$$\mathbf{A}\mathbf{t} = \mathbf{f} \qquad [1]$$
$$\mathbf{C}\mathbf{d} = \mathbf{e} \qquad [2]$$
$$\mathbf{G}\mathbf{e} = \mathbf{t} \qquad [3]$$

where $\mathbf{A}$ is the *equilibrium* matrix, which relates the internal bar tensions $\mathbf{t}$ to the applied nodal forces $\mathbf{f}$; the *compatibility* matrix $\mathbf{C}$ relates the nodal displacements $\mathbf{d}$ to the bar extensions $\mathbf{e}$ and the material equation introduces the axial bar stiffnesses along the diagonal of $\mathbf{G}$. It can be shown through a straightforward virtual work argument that $\mathbf{C} = \mathbf{A}^T$. The linear-elastic behaviour of the truss framework can now be described in terms of the vector subspaces of the equilibrium and compatiblity matrices [4]. In our case, of interest is the nullspace of the compatibility matrix, $\mathbf{C}\mathbf{d} = \mathbf{0}$, as it provides nodal displacements that, to first-order, are compatible with zero bar elongations.

The compatibility matrix is the Jacobian of the bar length constraints with respect to the nodal coordinates. This insight can be used to introduce additional equality constraints to the bar framework, such as dihedral angles between adjoining facets or fold lines. For instance, an angular constraint F can be set up in terms of the dihedral fold angle ϕ between two triangulated facets. Using vector analysis, the angle between two facets can be described in terms of cross and inner products of the nodal coordinates $\mathbf{p}$ of the two facets,

$$F = \sin\left(\phi\left(\mathbf{p}\right)\right) \qquad [4]$$

The Jacobian $\mathbf{J}$ then becomes

$$\mathrm{d}\phi = \frac{1}{\cos\left(\phi\right)} \sum \frac{\partial F}{\partial p_i} \mathrm{d}p_i = \mathbf{J}\mathbf{d} \qquad [5]$$

and can be concatenated with the existing compatibility matrix

$$\begin{bmatrix} \mathbf{C} \\ \mathbf{J} \end{bmatrix} \mathbf{d} = \begin{bmatrix} \mathbf{e} \\ \mathrm{d}\phi \end{bmatrix} \qquad [6]$$

where the $\mathrm{d}p_i$ are the elements of vector $\mathbf{d}$. The nullspace of this set of linear equations provides all nodal displacements $\mathbf{d}$ that do not extend the bars, and do not violate the specified angular constraints. For example, by constraining the bending of all facets, the single planar mechanism of the *Miura-ori* sheet can be found. A similar approach will be used to add tessellation boundary conditions to a single *Miura* unit cell.

Stiffness Equations. For a modal analysis of the folded *Miura* sheets, a stiffness formulation is necessary. Equations 1–3 can be combined into a single equation, relating external applied forces $\mathbf{f}$ to nodal displacements $\mathbf{d}$ by means of the material stiffness matrix $\mathbf{K}$.

$$\mathbf{K}\mathbf{d} = \mathbf{f} \qquad [7]$$
$$\mathbf{K} = \mathbf{A}\mathbf{G}\mathbf{C} = \mathbf{C}^T\mathbf{G}\mathbf{C} \qquad [8]$$

In fact, this approach can straightforwardly be extended to other sets of constraints by augmenting the compatibility matrix.

$$\mathbf{K} = \begin{bmatrix} \mathbf{C} \\ \mathbf{J} \end{bmatrix}^T \begin{bmatrix} \mathbf{G} & 0 \\ 0 & \mathbf{G}_J \end{bmatrix} \begin{bmatrix} \mathbf{C} \\ \mathbf{J} \end{bmatrix} \qquad [9]$$

In the case of the folded sheets, the additional stiffness terms on the diagonal of $\mathbf{G}_J$ can be the bending stiffness of the fold lines (K_{fold}) and facets (K_{facet}). Once the material stiffness
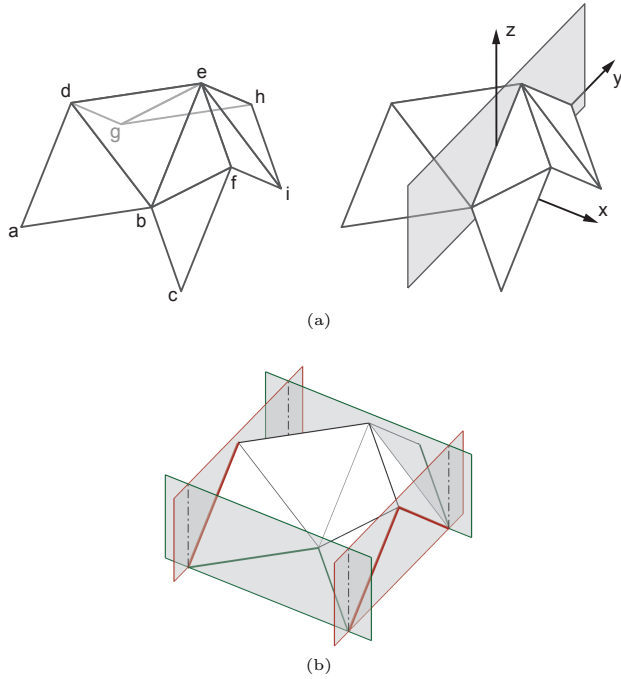
(a)

(b)

Fig. 2: The *Miura-ori* unit cell with additional fold lines diagonally across the facets. (a) The nodes are here labelled a–h with dihedral fold angles ϕ_{jk} (mountain fold, with respect to xy-plane, +ve). (b) The bounding planes visualise the tessellation boundary conditions, $\angle adg = \angle cfi$ and $\angle abc = \angle ghi$. The two sets of bounding planes are defined respectively by $\vec{dg} \times \vec{da}$, $\vec{fc} \times \vec{fi}$, and $(\vec{ba} \times \vec{bc}) \times \vec{ca}$, $(\vec{hg} \times \vec{hi}) \times \vec{gi}$.

matrix is formulated, a study of its eigenvalues and eigenmodes will reveal the softest, and therefore most dominant, deformation modes of the folded sheets. In [5] the dependence on the ratio $K_{\text{facet}}/K_{\text{fold}}$ and fold angle θ was studied for a 4×4 *Miura-ori* sheet with $\gamma = 60°$ and $a/b = 1$. To model rigid origami folding, the axial stiffness of the bars was taken to be several order of magnitude (actually, 10^6) greater than the bending stiffness for the facets and folds.

Coordinate Transformation. In the pin-jointed framework approach, all properties of the folded sheet are expressed in terms of the nodal coordinates. When studying the unit cell kinematics, the change in fold angle is more amenable to interpretation. A transformation matrix $\mathbf{T}$ converts nodal displacements $\mathbf{d}$ to changes in angle $\mathrm{d}\phi$:

$$\mathrm{d}\phi = \mathbf{T}\mathbf{d} \qquad [\mathbf{10}]$$

where $\mathbf{T}$ is the Jacobian of the angle constraint between two adjoining facets; see Eq. 5.

S3. Tessellated Unit Cell Kinematics

By adding tessellation boundary conditions to a single *Miura-ori* unit cell, the global sheet deformation modes can be studied. Shown in Fig. 2 is a unit cell, with tessellation boundary conditions visualised using bounding planes. The unit cell was formulated as a pin-jointed framework, with the additional boundary conditions:

$$\angle adg = \angle cfi \qquad [\mathbf{11}]$$
$$\angle abc = \angle ghi \qquad [\mathbf{12}]$$
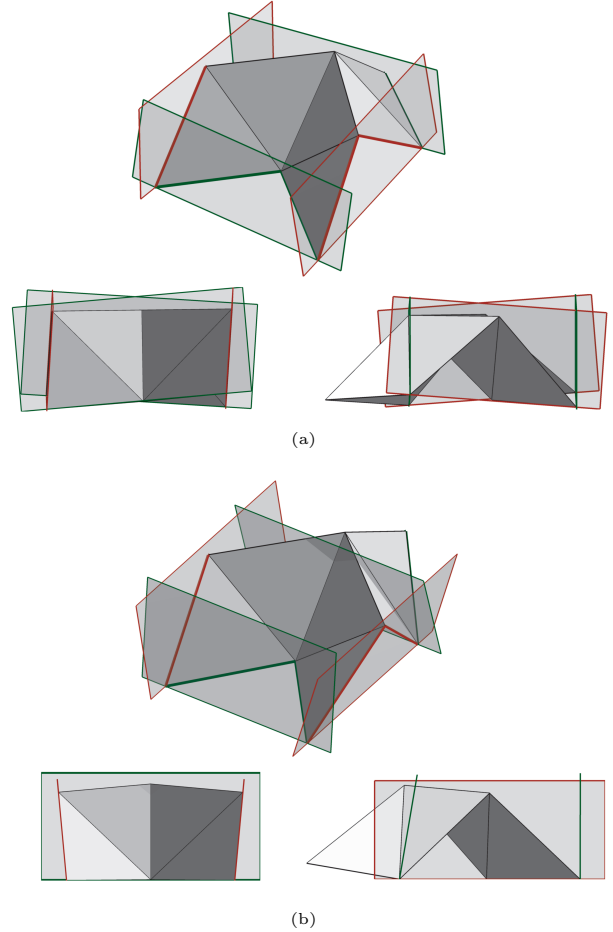

(a)

(b)

Fig. 3: The two out-of-plane deformation modes for the *Miura-ori* unit cell, with (a) the twisting and (b) the saddle-shaped mode.

These angle constraints were formulated in terms of the nodal coordinates, using straightforward vector equations. The Jacobian of these tessellation boundary conditions with respect to the nodal coordinates can be combined with the compatiblity matrix of the pin-jointed truss. The nullspace of the combined Jacobian provides a vector space of nodal displacements that, to first order approximation, satisfy both the bar length constraints and the tessellation boundary conditions.

The kernel of the Jacobian for the tessellated *Miura* unit cell has rank three, and therefore contains three independent deformation modes. All allowable unit cell deformations will be a linear combination of these three orthogonal modes. As the choice of base vectors of the nullspace is arbitrary, some further processing is required:

1. First, symmetry in the yz plane was imposed, by equating the change in facet folding angles: $d\phi_{bd} = d\phi_{bf}$ and $d\phi_{eg} = d\phi_{ei}$. The result is a set of two symmetric deformation modes.

   (a) The *planar mechanism* was found through a linear combination that preserves the planarity of facets. Folding takes place only along the fold lines.

   (b) Next, the symmetric subspace was orthogonalised with respect to the planar mechanism, using a QR-decomposition [7], to reveal the second symmetric de-

formation mode: *saddle-shaped bending*. Here folding takes place across all folds and facets. Note that all facet bending has the same sign, *i.e.* all facets deform either into a mountain or valley fold.

2. Second, the total nullspace was orthogonalised with respect to the symmetric modes. The final orthogonal mode is anti-symmetric: the *twisting* deformation mode. Here the change in fold angles $d\phi_{be} = d\phi_{eh} = 0$ due to symmetry considerations. The facet angles share the same sign on either side of the symmetry plane, but are anti-symmetric in the yz-plane: ϕ_{bf} and ϕ_{ie} both form mountain folds, while ϕ_{bd} and ϕ_{eg} are valley folds, or *vice versa*.

The resulting out-of-plane unit cell deformation modes are shown in Fig. 3. Note that the relationship between fold angles, facet bending, and unit cell geometry was here only studied numerically.
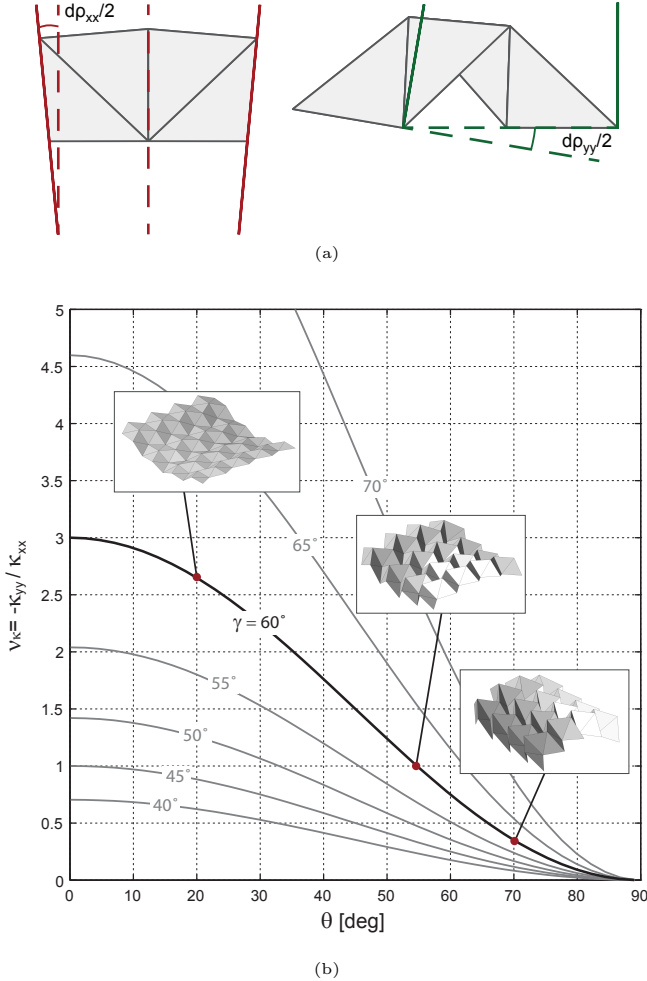

(a)

(b)

Fig. 4: (a) For the saddle-shaped deformation mode of the *Miura-ori* unit cell, the changes in curvature can be calculated using the tilt angles of the bounding planes: $\kappa_{xx} = d\rho_{xx}/2S$; $\kappa_{yy} = d\rho_{yy}/2L$. (b) The out-of-plane coupling coefficient $\nu_\kappa = -\kappa_{yy}/\kappa_{xx}$ is calculated for a range of geometries γ and fold angles θ; pictured are configurations with $\gamma = 60°$ and $a/b = 1$.

Curvature Calculation. From the three deformation modes, the various expansion and coupling coefficients can be calculated, using coordinate transformations of the nodal displacements. This can be achieved by looking at the translation (planar mode), tilting (bending mode) and rotation (twisting mode) of the bounding planes. Of primary interest is the coupling between the unit cell curvatures κ_{yy} and κ_{xx}. The curvatures can be calculated from the tilting of the bounding planes:

$$\kappa_{xx} = d\rho_{xx}/2S \qquad [13]$$
$$\kappa_{yy} = d\rho_{yy}/2L \qquad [14]$$

where $d\rho_{xx}$ and $d\rho_{yy}$ follow from the nodal coordinates. The out-of-plane coupling coefficient $\nu_\kappa = -\kappa_{yy}/\kappa_{xx}$ can then be calculated, and is plotted in Fig. 4.

S4. Manufacture of Miura-Folded Meta-Materials

To demonstrate the kinematics of the folded meta-materials, examples of *Miura*-folded shell structures and cellular meta-materials were constructed. A stack of *Miura*-folded layers made of card, and a single *Miura-ori* sheet folded from stainless steel are shown in Fig. 5 and Fig. 6 respectively.

While paper can be manipulated manually to form the *Miura-ori* layers, making folded sheets from materials such as steel requires specialised manufacturing methods. Two challenges must be overcome: due to the inherent folding kinematics it is difficult to simultaneously have both folded and unfolded regions in the sheet material; and during the folding process from a flat sheet, the sheets contract in-plane whilst expanding in thickness. Schenk [5] provides a review of manufacturing methods that aim to solve these problems.

Cold Gas Pressure Folding We here summarise the method used to manufacture the stainless steel *Miura*-folded sheet from Fig. 6. The method is based on that developed in [6], and is particularly suited for prototyping purposes as it requires minimal tooling.

To assist folding, the sheets are first locally weakened along the fold lines. This can be achieved by locally thinning the material along the fold lines by chemical etching. Fig. 7(a) shows a stainless steel sheet (0.2 mm thickness) with the fold pattern (3 mm wide fold lines) etched through half of the sheet thickness. The mountain and valley folds were etched on opposite sides of the sheet; as a result, where the fold lines meet at the vertices, the material was completely removed. This is desirable, in order to avoid complex material deformations at the vertices. Next, a series of freely hinged spacers (consisting of metal plates joined together with adhesive tape to provide the hinge) are placed along the fold lines of the etched plate; see Fig. 7(b). A second identically etched plate is placed on top of the spacers, parallel with the first sheet. The combination is packed into an air-tight bag, which connected to a vacuum pump; Fig. 7(c). As the air is removed, the resulting pressure difference bends the material along the fold lines; see Fig. 7(d). The biaxial contraction during the folding process is enabled by the freely hinging spacers. The fold depth is limited by the eventual contact between the two sheets, which is determined by the height of the spacers.

The manufacturing process produced an accurately folded sheet with no material deformation, other than bending along the fold lines. When manufacturing deeper sheets, as would be required for layers B in the stacked meta-material configuration, some issues were encountered. Folding had to be continued manually to the desired depth, and the resulting inaccuracies prevented the stacking of the stainless steel *Miura-ori* layers.

References

1. Seffen KA (2012) Compliant Shell Mechanisms. *Philosophical Transactions of the Royal Society A: Mathematical, Physical and Engineering Sciences* 370(1965):2010–2026.
2. Duncan JP, Duncan JL (1982) Folded Developables. *Proceedings of the Royal Society A* 383(1784):191–205
3. Guest SD (2006) The stiffness of prestressed frameworks: A unifying approach. *International Journal of Solids and Structures* 43(3–4):842–854
4. Pellegrino S, Calladine CR (1986) Matrix analysis of statically and kinematically indeterminate frameworks. *International Journal of Solids and Structures* 22(4):409–428
5. Schenk M (2011) Folded Shell Structures, Ph.D. thesis, University of Cambridge.
6. Schenk M, Allwood JM, Guest SD (2011) Cold Gas-Pressure Folding of Miura-ori Sheets. *Proceedings of the International Conference on Technology of Plasticity (ICTP 2011), Aachen, Germany*, pp. 459–464.
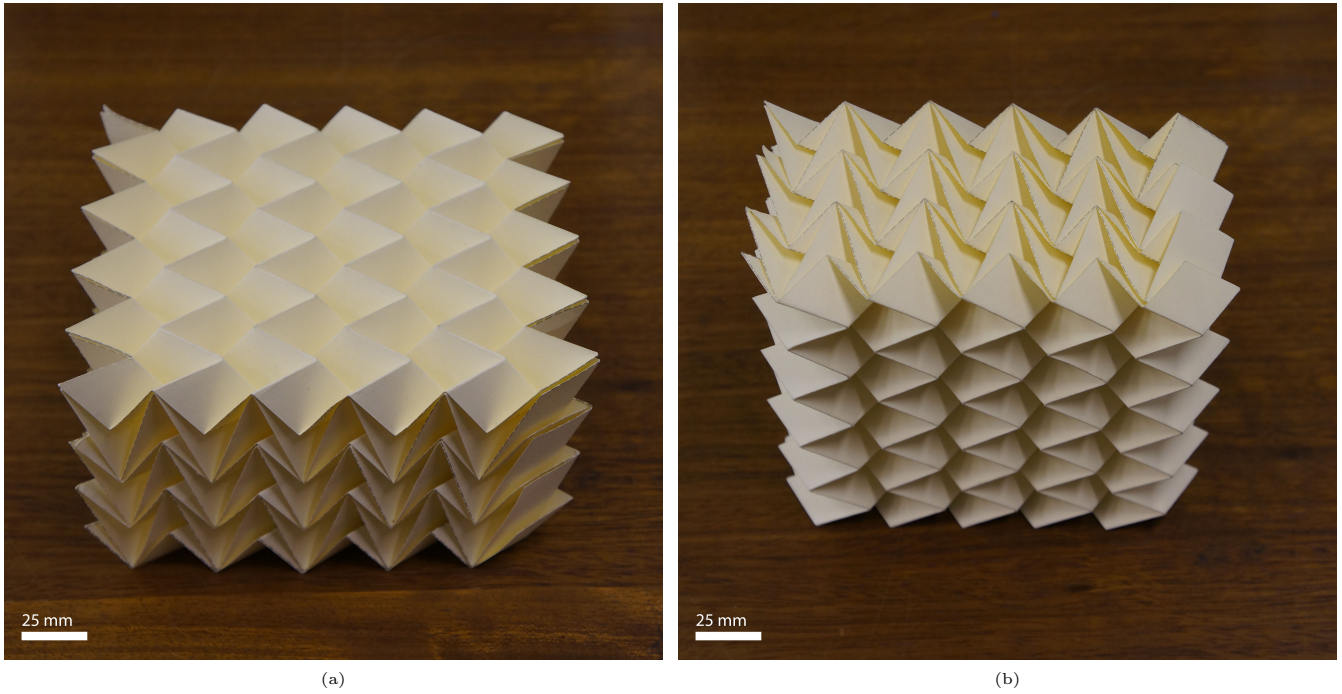7. Strang G (1988) *Linear Algebra and its Applications* (Harcourt Brace Jonanovich), Third Edition.

Fig. 5: A folded cellular meta-material constructed from card (200 gsm). The individual *Miura-ori* layers were manually scored and folded. Dimensions of the tessellated unit cells are $a = b = 25$ mm and $\gamma = 60°$.
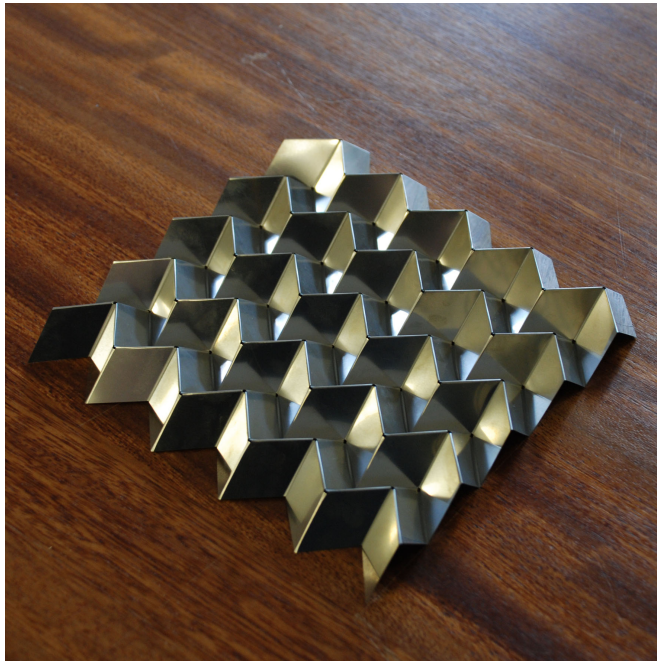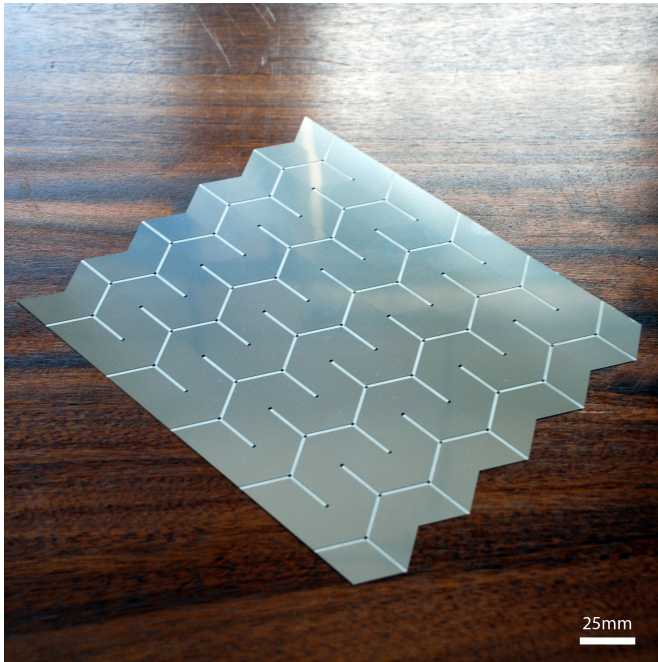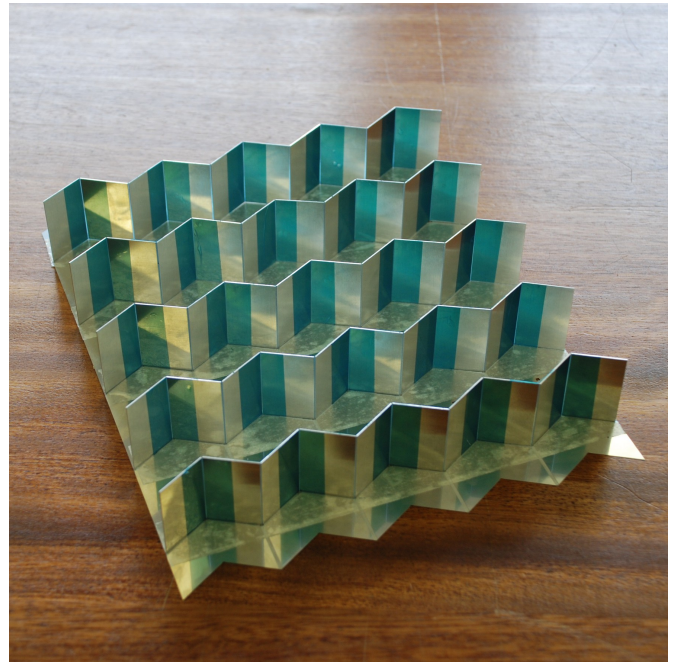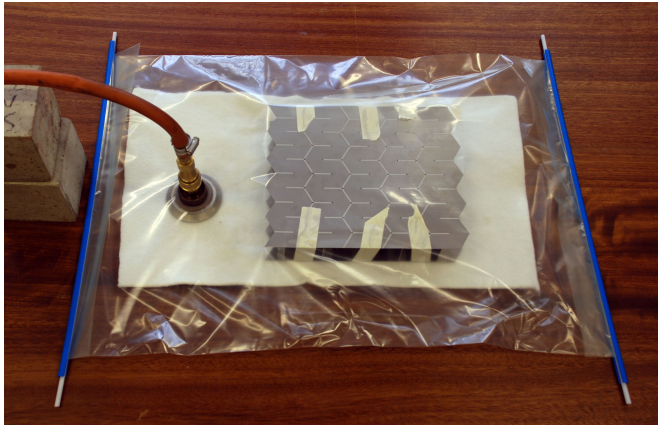
Fig. 6: A *Miura-ori* sheet of 0.2 mm stainless steel, manufactured using a cold gas pressure folding technique. To facilitate folding, at the fold lines the material is locally thinned by means of chemical etching.
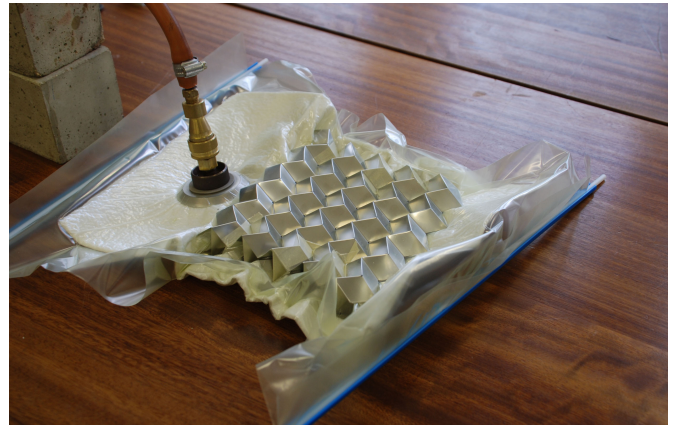
Fig. 7: Manufacturing process of a *Miura-ori* sheet using a cold gas pressure folding technique: (a) the 0.2 mm stainless steel sheet is locally thinned at the fold lines by chemical etching, to facilitate the folding; (b) freely hinged spacer plates are placed along alternating ridges, before a second identically etched sheet is placed on top; (c) the combined sandwich is placed inside an airtight bag connected to a vacuum pump; (d) after evacuating the air from the bag, the two *Miura-ori* sheet fold automatically along the fold lines.